

# Watching (De)Intercalation of 2D Metals in Epitaxial Graphene: Insight into the Role of Defects

Falk Niefind, Qian Mao, Nadire Nayir, Malgorzata Kowalik, Jung-Joon Ahn, Andrew J. Winchester, Chengye Dong, Rinu A. Maniyara, Joshua A. Robinson, Adri C. T. van Duin,\* and Sujitra Pookpanratana\*

Intercalation forms heterostructures, and over 25 elements and compounds are intercalated into graphene, but the mechanism for this process is not well understood. Here, the de-intercalation of 2D Ag and Ga metals sandwiched between bilayer graphene and SiC are followed using photoemission electron microscopy (PEEM) and atomistic-scale reactive molecular dynamics simulations. By PEEM, de-intercalation “windows” (or defects) are observed in both systems, but the processes follow distinctly different dynamics. Reversible de- and re-intercalation of Ag is observed through a circular defect where the intercalation velocity front is  $0.5 \text{ nm s}^{-1} \pm 0.2 \text{ nm s}^{-1}$ . In contrast, the de-intercalation of Ga is irreversible with faster kinetics that are influenced by the non-circular shape of the defect. Molecular dynamics simulations support these pronounced differences and complexities between the two Ag and Ga systems. In the de-intercalating Ga model, Ga atoms first pile up between graphene layers until ultimately moving to the graphene surface. The simulations, supported by density functional theory, indicate that the Ga atoms exhibit larger binding strength to graphene, which agrees with the faster and irreversible diffusion kinetics observed. Thus, both the thermophysical properties of the metal intercalant and its interaction with defective graphene play a key role in intercalation.

not present in their bulk analogs. For instance, heterostructures of 2D transition metal dichalcogenides have potential applications in many optoelectronic technologies such as photodetectors, light emitting diodes, and plasmonics, due to the ultrafast photoresponse of their excitons.<sup>[1]</sup> Enhanced plasmonic properties were recently observed in 2D silver (Ag) intercalated in epitaxial graphene (EG), where the graphene confines and stabilizes Ag in the 2D form.<sup>[2]</sup> Superconductivity was observed in 2D gallium that was also intercalated in epitaxial graphene.<sup>[3,4]</sup>

While heterostructures of 2D materials provide design options for materials and device engineering for functionality, they suffer from limited scalability. Mechanically transferring 2D materials from bulk crystals to arbitrary materials (i.e., “transfer and stack”) is highly appealing and ubiquitous due to their van der Waals forces and has enabled formations of many heterointerface combinations.<sup>[1]</sup> However, this procedure is not scalable and

would limit commercial use of technologies based on 2D heterostructures. Large area, epitaxial graphene can be routinely grown on SiC substrates and serves as a promising template to form atomically-thin heterostructures.<sup>[5]</sup> Since the fabrication

## 1. Introduction

Atomically-thin 2D materials and their heterostructures offer new physical and chemical properties that are

F. Niefind, J.-J. Ahn, A. J. Winchester, S. Pookpanratana  
Nanoscale Device Characterization Division  
National Institute of Standards and Technology  
Gaithersburg, MD 20899, USA  
E-mail: sujitra@nist.gov

F. Niefind  
Department of Chemistry & Biochemistry  
University of Maryland  
College Park, MD 20742, USA

Q. Mao, N. Nayir, M. Kowalik, A. C. T. van Duin  
Department of Mechanical Engineering  
Pennsylvania State University  
University Park, PA 16802, USA  
E-mail: acv13@psu.edu

N. Nayir  
Department of Physics  
Karamanoglu Mehmetbey University  
Karaman 70000, Turkey

J.-J. Ahn  
Department of Physics  
Georgetown University  
Washington, DC 20057, USA

A. J. Winchester  
Institute for Soft Matter  
Georgetown University  
Washington, DC 20057, USA

C. Dong, R. A. Maniyara, J. A. Robinson  
Department of Materials Science & Engineering  
Pennsylvania State University  
University Park, PA 16802, USA

 The ORCID identification number(s) for the author(s) of this article can be found under <https://doi.org/10.1002/sml.202306554>

DOI: 10.1002/sml.202306554

of epitaxial graphene, intercalation of gases,<sup>[2,6–9]</sup> metals,<sup>[2,7,10,11]</sup> and semi-metals<sup>[7–9,11]</sup> have been widely pursued as a method to form heterostructures. Intercalation can influence the electronic properties of the graphene by decoupling it from the substrate, which in turn can impact the effective carrier concentration of the graphene. For instance, different intercalants can change the majority carrier in epitaxial graphene from n-type to p-type<sup>[2]</sup> or a balanced carrier.<sup>[12]</sup> Intercalation is mostly done in high or ultrahigh vacuum environments in a two-step sequence where the intercalant is physically deposited or introduced to the epitaxial graphene, and then the whole structure is annealed at elevated temperatures to drive the intercalant between the graphene and SiC. Recently, confinement heteroepitaxy (CHet) was introduced as a new “one-step” intercalation method for 2D metals at the EG/SiC interface at elevated pressures and temperatures and has successfully produced 2D Ga, In, Ag, and Sn.<sup>[3]</sup> In the CHet process, controllable defects in monolayer epitaxial graphene (EG), acting as the entry for metals into EG/SiC interface, are generated via oxygen plasma treatment. Then metallic atoms, vaporized from metallic precursors, go through the defects, and stabilize due to high-energy EG/SiC interface and the formation of strong metal-SiC bondings.

While intercalation, including CHet, is a common procedure to create atomically thin 2D heterostructures, the atomic-level understanding of the intercalation mechanism remains elusive and multiple mechanisms have been proposed. A few of the mechanisms proposed involve defects in the graphene. Full-field imaging techniques are best suited to follow dynamic processes and to glean insight into the (de)intercalation process. Low energy (LEEM) and photoemission electron microscopy (PEEM) have proven valuable to directly observe (de)intercalation processes.<sup>[13–21]</sup> Observations that the intercalation processes proceeds at domain boundaries,<sup>[13,15,17–20]</sup> terrace edges,<sup>[22]</sup> cracks,<sup>[16]</sup> or wrinkles<sup>[21,23]</sup> further support the role of defects serving as gates for a variety of epitaxial graphene systems (i.e., on SiC, Ir, Ru). There are some mechanisms that propose that the intercalant penetrates through the graphene,<sup>[14–16]</sup> but this process could be enabled by vacancy defects in the graphene.

Recently, several studies have also shown that defects in the epitaxial graphene layer serve as gates through which intercalant atoms can enter and go between the EG/SiC interface.<sup>[3,15,19–21,23–27]</sup> The CHet process exploits these defects, and it has been shown that pre-treating EG with O<sub>2</sub>/He plasma increases the area of intercalated 2D metal.<sup>[3]</sup> The plasma treatment induces the formation of large-sized carbon vacancies in EG. The theoretical studies propose that oxygen-containing surface functional groups weaken the binding strength between the metal intercalant and graphene by partially passivating defects, thus facilitating metal adhesion and diffusion to the graphene-SiC interface.<sup>[3,25]</sup> However, the direct observation of this intercalation process, where does the intercalant enters and how it proceeds, has not been performed.

In this work, the defect-driven de-intercalation mechanisms of 2D Ag and Ga at the SiC/EG interface are unraveled using the combination of in-situ PEEM measurements, reactive force-field (ReaxFF) molecular dynamics simulations, and Density Functional Theory (DFT) calculations. These two systems are the focus of our study here since they have been repeatedly shown to form large area 2D metals that are 2–3 atomic layers thick and

induce unique physical properties as nanoscale heterostructures (i.e., plasmonics for 2D Ag,<sup>[2]</sup> superconductivity in 2D Ga<sup>[3]</sup>). While both systems are initially intercalated using CHet, we propose that the different appearance of the defects during de-intercalation is due to the specific intercalant-graphene interaction which may heal defects differently. In the 2D Ag system, both the de-intercalation and re-intercalation processes are observed, and this semi-reversible process is supported by calculations. In the 2D Ga system, only de-intercalation is observed due to the low melting temperature of Ga, and the process is kinetically faster with dependencies on the defect shape. MD predicts that the thermophysical properties of the Ga atoms influence the complex de-intercalation mechanism, with an intermediate diffusion process between graphene layers before complete de-intercalation. By tracking and modeling the process in both 2D metal systems, the mechanism of intercalation is proposed based on the role of defect healing dependent on the properties and interaction of the specific intercalant with graphene.

## 2. Results and Discussion

The de-intercalation process of 2D Ag is first observed in PEEM images taken before and after in situ annealing at 436 K, as shown in **Figure 1a,b**, respectively. This heating procedure is typically used to remove adsorbates in UHV; however, the number of small bright features substantially increased after annealing (**Figure 1b**). AFM images further confirm that the Ag atoms represented by the bright (high intensity) features observed in the PEEM (**Figure 1a–c**) are at the topmost surface (**Figure 1d**) on multiple regions on the sample. The average height of these features is  $15.2 \text{ nm} \pm 2.1 \text{ nm}$  (**Figure 1e**), and they have a relatively flat surface (average roughness,  $R_q$ , of  $0.39 \text{ nm} \pm 0.14 \text{ nm}$ ) and steep sidewalls (slope:  $100 \text{ nm } \mu\text{m}^{-1} \pm 20 \text{ nm } \mu\text{m}^{-1}$ ). While graphene is known to be able to cover particles,<sup>[28]</sup> the steep incline of the flanks of all four particles within **Figure 1d** indicates that the silver particles are on top of and not covered by graphene. The elemental composition of these particles are confirmed as being primarily composed of Ag ( $88\% \pm 10\%$ ) by SEM-EDX measurements (**Figure 1f**; EDX spectra in **Figure S1**, Supporting Information). In **Figure 1g**, the observation of de-intercalation is further confirmed by laterally-integrating XPS where the presence of Ag on the sample surface increased by an intensity factor of 100 after in situ PEEM annealing.

After the bright, 3D structures are identified as being primarily composed of silver, further de- and subsequent re-intercalation of Ag atoms are tracked at temperatures up to 575 K for multiple regions of interest (ROI) (**Figure 2a**) during in situ annealing in the PEEM. Based on the initial observation at 436 K, the temperature range could be reasonable to follow the movement of Ag atoms. **Figure 2b,c** show representative snapshots of ROI 1 in **Figure 2a**, from the first and second annealing cycles, respectively. Difference images in **Figure 2d,e** highlight the regions of increased (in green) and decreased (in red) intensity from **Figure 2b,c**, respectively, illustrating the regions of the Ag de- and re-intercalation. In the beginning of cycle 1, an increasing amount of green regions are observed, indicating areas where the Ag de-intercalation takes place. The trend reverses at later times as red regions occur, indicating a decrease in the size of the silver structure. This observation is corroborated by integrating the normalized intensity

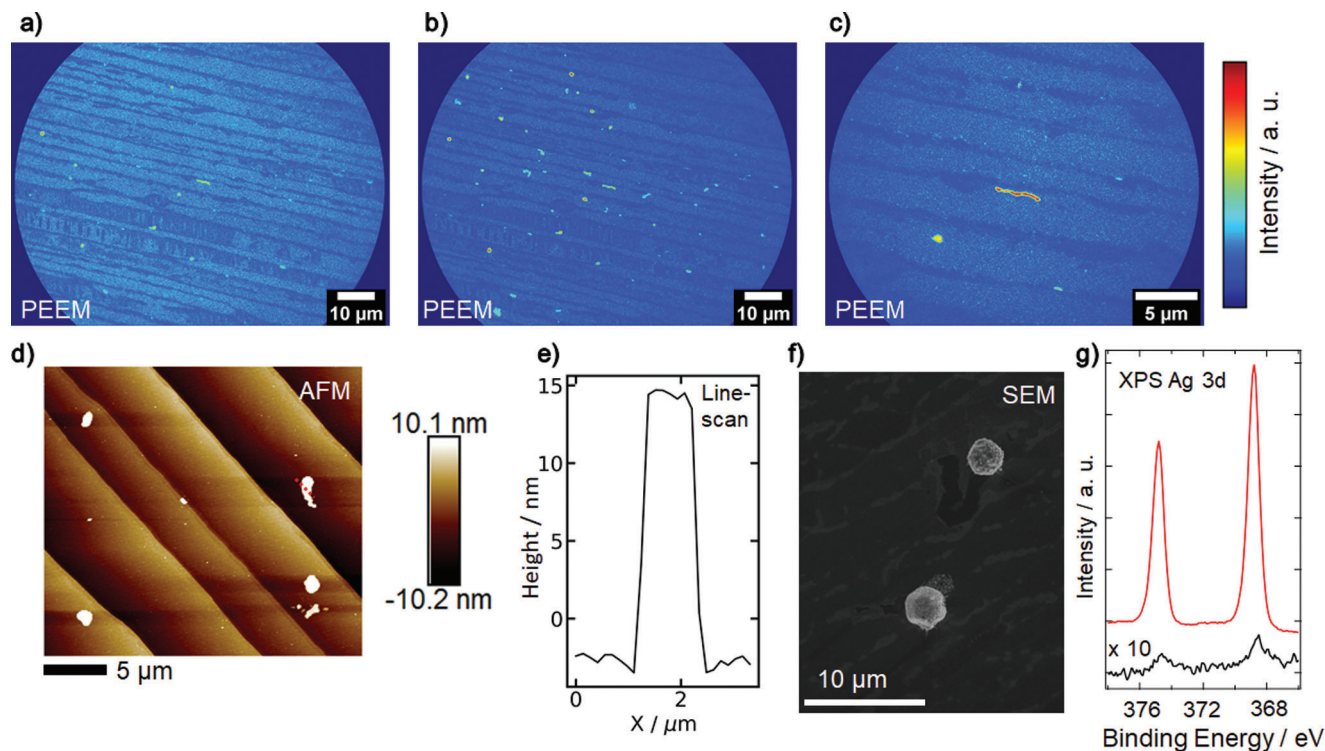


**Figure 1.** PEEM images of the same Gr/Ag/SiC sample a) before and b) after in situ heating that show an increase in bright particles. In (c) higher magnification image as seen in (a). The AFM topography (d) and line scan (e) shows that the particles are on top of the graphene. The topographic line scan is extracted along the red dashed line in (d). Composition of the particles as silver are confirmed by f) SEM-EDX image and g) XPS Ag 3d spectra of Gr/Ag/SiC sample that did (red, top) and did not (black, bottom) undergo in situ PEEM annealing. The EDX data is in Figure S1 (Supporting Information).

within ROI 1 as a function of time, shown together with the temperature profile during the annealing cycle in Figure 2f. In cycle 1, there is an increase in PEEM intensity in the time interval of 10 to 31 min (corresponding to temperatures from 405 to 493 K). This de-intercalation is followed by a period with little to no change in PEEM intensity from 32 to 53 min. The beginning of the re-intercalation is coincidentally observed at the end of the first in situ heating cycle (from 54 min until 62 min).

The re-intercalation of Ag resume at elevated temperatures during annealing cycle 2 until the Ag structure completely disappears (far right panel in Figure 2c). Figure 2g shows that after an initial warm-up period of  $\approx 25$  min, the intensity of ROI 1 decreases linearly while the sample temperature reaches 494 K, and eventually the Ag particle disappears. After in situ annealing cycle 2, the de- and re-intercalations are no longer observable even at temperatures above 586 K which indicates that the process is not continuously reversible. The linear decline in PEEM intensity is observed in six other ROI labeled in Figure 2a and shown in detail in Figure S2b and Video S1 (Supporting Information). By imaging the time-dependent change of the Ag structures, the intercalation windows are identified for seven ROI in the supplemental video. ROI 2 and 4 show a substantial decrease in intensity than the other ROI (see Table S1, Supporting Information). These ROI contained two distinct intercalation windows for the Ag structures to re-intercalate beneath the graphene which contributes to the increased rate of intercalation. The other five ROI showed one intercalation window. The linear behavior of the de-

creasing PEEM intensity of the Ag particles with increasing time and increasing temperature suggests a zero-order kinetic process, where the intercalation speed is independent of the concentration (i.e., size) of the Ag structures. Zero-order kinetics are generally considered to be a special case of higher order processes that are constrained by a rate limiting step,<sup>[29]</sup> which we propose to be the intercalation windows. The CHet intercalation method creates large-sized defects in graphene via plasma exposure that promotes intercalation of metal atoms toward the graphene-SiC interface, and these defects do not completely heal after the intercalation process.<sup>[3]</sup> We surmise that the intercalation windows observed in the PEEM measurements are co-located at defective regions of graphene as also proposed by previous studies.<sup>[3,24,25]</sup>

Imaging these intercalation windows allows for insight into their locations and intercalation dynamics to be gleaned. Some of the intercalation windows were found to be closer to the terrace edge or the center of terraces (Figure 2a; Figure S2c, Supporting Information), but not directly at the terrace step. We expect that defects in epitaxially-grown graphene prefer to concentrate in the proximity of structural defects such as terrace step edges<sup>[30]</sup> that suggests that the location of intercalation windows here originates from another source. The Ag intercalation speed is estimated, by combining the PEEM and AFM data (Figure S3, Supporting Information), as  $1.3 \times 10^5$  atoms  $s^{-1}$  and its corresponding velocity front as  $0.5 \text{ nm s}^{-1} \pm 0.2 \text{ nm s}^{-1}$ . The intercalation speed of Ag is comparable to hydrogen

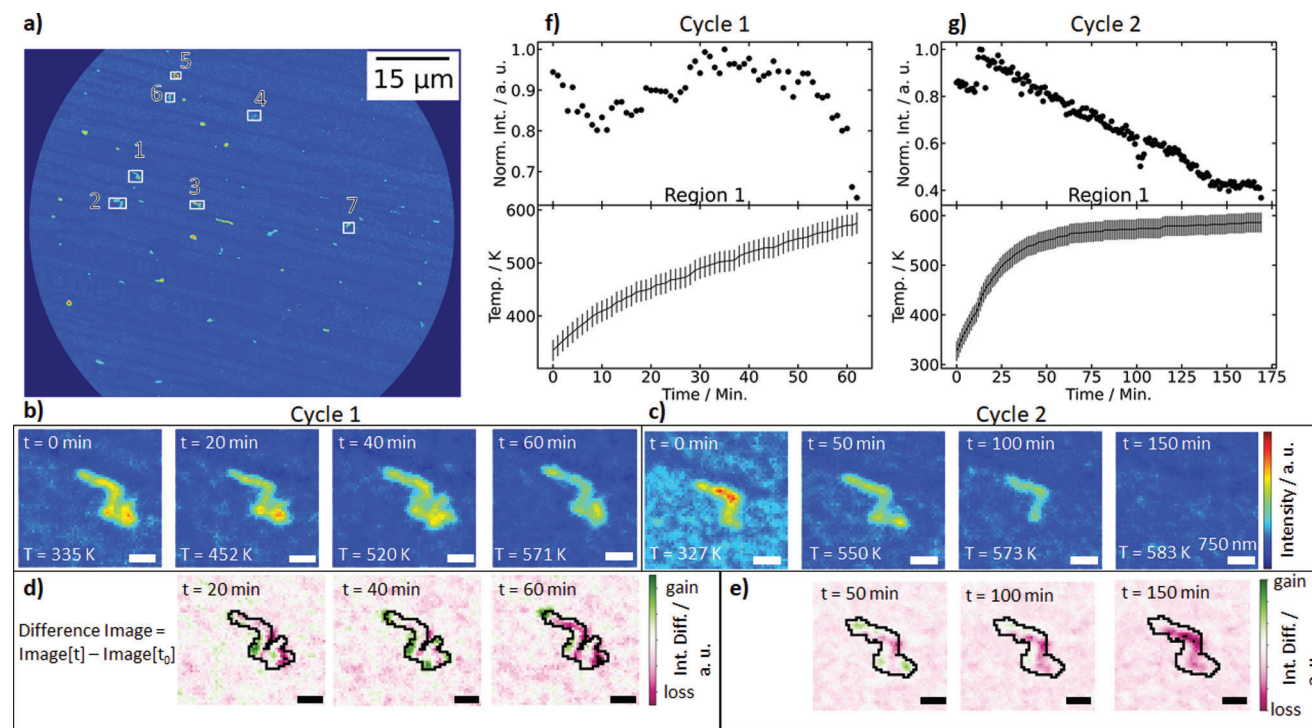


**Figure 2.** PEEM images during in situ annealing of Gr/Ag/SiC at  $\approx 583$  K. In (a) multiple regions of interest (ROI) are identified that change in intensity during annealing processes. ROI 1 is shown in more detail in (b) the first and (c) second annealing cycles and its difference images are shown in (d,e) indicating the de- (green) and re-intercalation (red) of the Ag structure. The integrated and normalized intensity of ROI 1 and sample temperature are plotted against time for annealing (f) cycle 1 and (g) cycle 2. The black outlines in (d,e) are a guide to the eye. The error bars in (f,g) are due to the uncertainty of the range in the thermocouple reading between the sample surface and thermocouple junction. The scale bar is 750 nm for (b–e).

de-intercalation that was reported between  $0.1 \text{ nm s}^{-1}$  and  $95 \text{ nm s}^{-1}$ .<sup>[20]</sup> The intercalation speed is faster than in-plane diffusion between graphenic sheets, where Gan et al. observed in-plane Au diffusion with an average speed of  $\approx 0.01 \text{ nm s}^{-1}$ .<sup>[31]</sup>

Now, we turn to the Gr/Ga/SiC system, which exhibits considerably different de-intercalation dynamics compared to the Gr/Ag/SiC system. For this system, due to the low melting temperature of Ga, caution was taken to continuously record PEEM images while slowly raising the sample temperature until changes at the surface were observed. **Figure 3a** shows a PEEM image of three representative regions (ROI 1 to 3 highlighted with dashed red lines) with varying PEEM intensities during in situ annealing at  $\approx 609$  K. In **Figure 3b**, a representative distinctly-shaped, bright feature is shown (ROI 1 in **Figure 3a**) where the bright regions grow with increasing PEEM intensity and some eventually coalesce (see Video S2, Supporting Information) as time and temperature increase. It is noteworthy that the de-intercalation process abruptly starts (i.e., burst-like) in distinct regions and grows with increasing time until the process is completed. This burst-like feature observed here is similar to the intercalation of germanium<sup>[19]</sup> and cesium<sup>[21]</sup> into the Gr/SiC interface. This behavior is also observed in ROI 2 and several others (**Figure S5** and Video S2, Supporting Information). In contrast, there are regions that show opposite trends—the PEEM intensity decreases homogeneously in ROI 3 (**Figure 3c**). These changes in PEEM intensity are shown in **Figure 3d** where the normalized intensities of ROI 1–3 are integrated against the time during the

in situ annealing (the temperature profile during the process is shown in the bottom panel). The behavior in these bright regions (e.g., ROI 1 in **Figure 3**) differs from the low-intensity regions (e.g., ROI 3 in **Figure 3**) during the in situ annealing process. For example, the intensity of bright features in ROI 1 initially shows little to no change, and then abruptly increases (see also in **Figure S5b**, Supporting Information). However, this trend is converse in the low intensity regions such as ROI 3, where for the first 25 min of the in situ annealing, the intensity linearly decreases and then transitions into a sharp decline at  $\approx 35$  min. The trend in the low intensity regions (e.g., ROI 3 in **Figure 3**) follows a path of nucleation and coalescing that is similar to the de-intercalation of germanium,<sup>[19]</sup> cesium,<sup>[21]</sup> and hydrogen<sup>[20]</sup> from a Gr/SiC interface. Here, the de-intercalation and loss of gallium are confirmed ex situ after the PEEM measurements. The XPS measurements on the Gr/Ga/SiC samples that did (in red) and did not undergo (in black) in situ annealing in PEEM are compared in **Figure 3e**. After the annealing process, the Ga signal decreased by 85%, which indicates a significant amount of Ga is removed from the Gr/Ga/SiC system. Partial de-intercalation is also supported by the C 1s XPS (see **Figure S6a**, Supporting Information).

The change in photoemission intensity is directly related to the concentration of intercalants, and the abrupt “step-like” function transition in **Figure 3d** (top two panels) was recently reported in magnesium intercalating at the Gr/SiC interface.<sup>[32]</sup> Similarly, we can gain insight into the Ga de-intercalation dynamics by fitting the data to a logistic (or

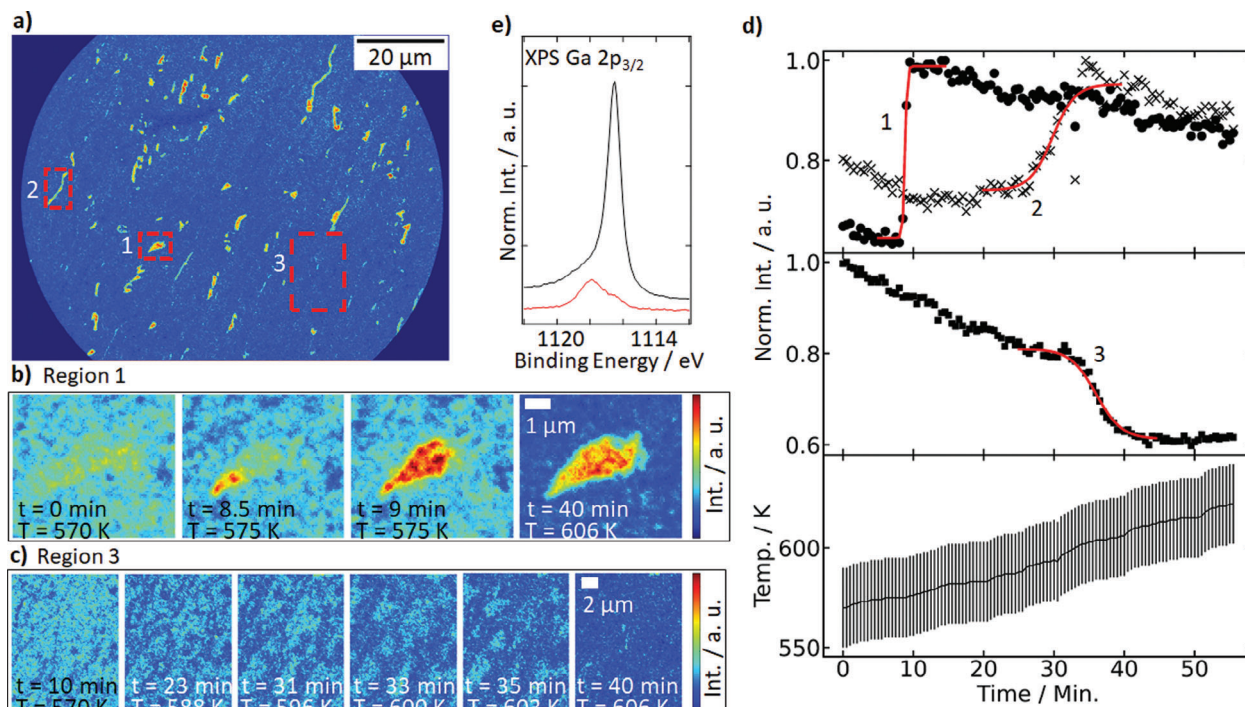


**Figure 3.** PEEM images during in situ annealing of Gr/Ga/SiC at  $\approx 609$  K. In (a) multiple regions of interest (ROI) are identified that change in intensity during annealing process. ROI 1 and 3 are shown in more detail at different temperatures (and times) in (b,c), respectively. In (d), the PEEM intensity of ROI 1 (filled circles), 2 (crosses), and 3 (filled squares) are plotted against time and the bottom most panel shows the sample temperature (with the uncertainty range of thermocouple) during the in situ annealing process. In (d), the fit of the logistic function (Equation (1)) is shown as solid red lines. In (e), XPS of the Gr/Ga/SiC sample that did (red, bottom) and did not (black, top) undergo in situ PEEM annealing are shown.

Verhulst) function that is a model used for self-limiting processes. We fit the sharp decline in our data to the logistic function (Equation (1)),

$$f(t) = \frac{a}{1 + e^{-c(t-d)}} + b \quad (1)$$

where  $a$  represents the maximum value of the curve,  $b$  the offset,  $c$  the growth rate (or steepness of the function),  $t$  the time, and  $d$  the midpoint (or onset) of the sigmoid. The fits to ROI 1–3 are shown in Figure 3d as solid red lines. Fitting results of the eight bright and five low intensity features in Figure 3a are shown in Figures S4 and S5 (Supporting Information) and summarized in Tables S2 and S3 (Supporting Information). Both the growth rate ( $c$ ) and onset ( $d$ ) of the bright regions (e.g., ROI 1, 2) varied between  $0.62$ – $12.16 \text{ min}^{-1}$  and  $6.9$ – $31.8$  min, respectively. In contrast, the low intensity regions (e.g., Region 3) have a smaller range in growth rate and onset as  $0.55$ – $1.51 \text{ min}^{-1}$  and  $34$ – $36$  min, respectively. For the low-intensity regions, the growth rate and onset show a slight variation between different regions, which suggests homogeneity while the intensity transition occurs over a longer time span (smaller growth rate). We observe a variation in the growth rate and time onset for different bright features (Figure 3d (top); Figure S5b, Supporting Information). The growth rate varies and tends to be larger than that of the low intensity feature. Analyzing the aspect ratios (long side divided by short side) of the different bright regions and plotting them against the respective onset temperatures (Figure S5c, Support-

ing Information), we find that elongated topographic features have delayed onset times. We propose that the homogeneous, low-intensity regions (like ROI 3 in Figure 3a) contain Ga diffusing toward these windows (i. e., ROI 1 and 2 in Figure 3a), where Ga escapes from the graphene system. The windows likely consist of a high density of multivacancy defects that kinetically favor the de-intercalation of Ga.<sup>[25]</sup>

The contrasting de-intercalation dynamics between the 2D Ag and 2D Ga system raises the question on the physical origin of these differences. The 2D Ag de-intercalation is kinetically slower and the apparent size of the intercalation window is much smaller when compared to the 2D Ga system. The Ag de- and re-intercalate, allow us to calculate the silver front speed, which is not possible for the Ga system since the process is faster and the loss is more homogeneous over the sample surface. The Ag demonstrates the capability to de-intercalate and re-intercalate multiple times, while the Ga only de-intercalates. These observations suggest the differences are due to: 1) thermophysical properties of the intercalants, and 2) the intercalant—defective graphene interactions.

DFT calculations are performed to determine the binding strength of a metal intercalant to the plasma-treated defective graphene, thus, to gain thermodynamic insight on the de- and re-intercalation processes of these 2D systems. First, COH, COC and CO = functional groups are introduced in defective graphene to mimic the plasma-treated surface. Metal atoms are deposited on a defective graphene in the proximity of these functional groups, and the metal intercalant binding energies to these

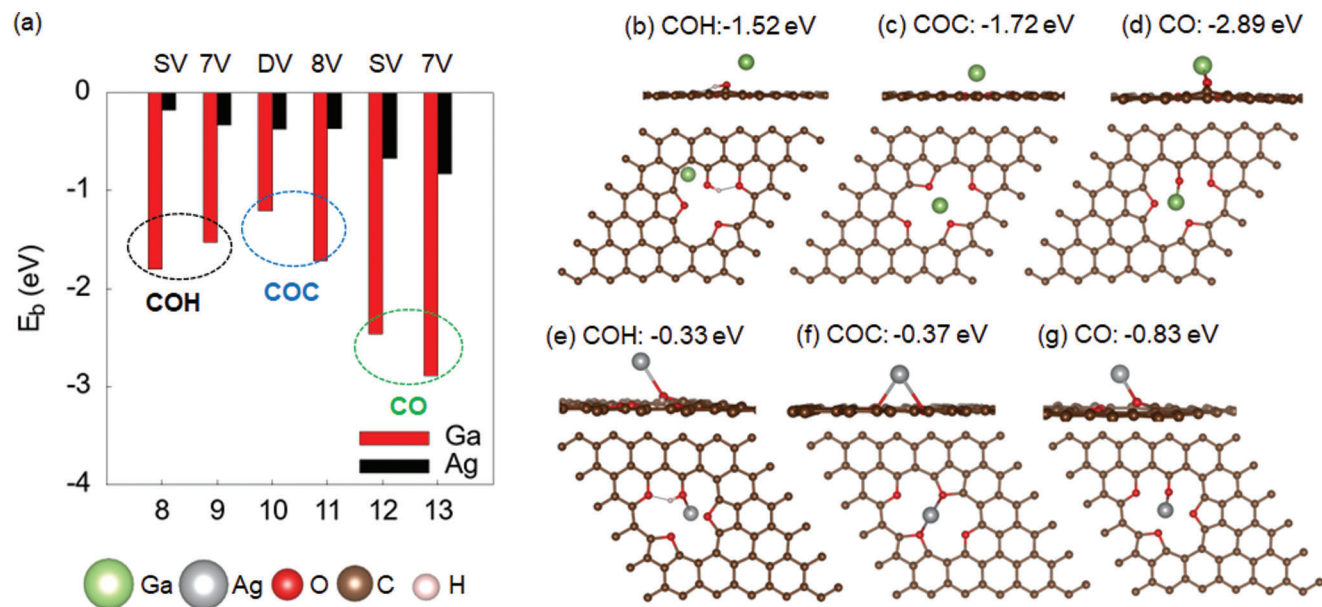


**Figure 4.** DFT predicted comparative a) binding energies ( $E_b$ ) of Ag and Ga to defective graphene with COH, COC, and CO = functional groups for different vacancies. Atomistic illustrations of stable configurations of b–d) Ga and e–g) Ag atoms interacting with functionalized defective graphene. The defective graphene is represented as single (SV), double (DV), hepta- (7 V) and octa- (8 V) vacancies.

defects are determined (Figure 4a). As seen in Figure 4 and Figure S7 (Supporting Information), the presence of COC and COH groups on the surface significantly weakens the interactions between Ag and the graphene surface where binding energies to graphene vary between 0.18 to 0.37 eV (Figure 4a), and this is consistent with the previous work for other metals.<sup>[3,33]</sup> This indicates the physisorption of Ag to the surface with COC and COH groups present, facilitates the Ag re- and de-intercalating through graphene. The presence of these functional groups are also supported by the XPS analysis in Figure S1e,f (Supporting Information). Among the functional groups considered, the CO = group exhibits the strongest attraction toward the Ag metal. On the other hand, regardless of the type of functional groups, the binding strength of Ga to graphene is stronger than that of Ag to graphene. In Figure 4a, the corresponding binding energies fall in the range of 1.2 to 2.9 eV and indicative of the chemisorption of Ga to the defective graphene surface, contrary to the Ag case.

The trend is supported by the ReaxFF-predicted binding energies, which are complementary to the DFT results due to the ability of ReaxFF to model complex systems on a large scale. A mono-, tetra-, and trideca-vacancy are introduced on each graphene layer of Gr/metal/SiC system (Figure S8a–c, Supporting Information), and the binding energies of a metal to different adsorption sites on graphene (i.e., above, below, and between graphene layers) with various vacancy defects are computed. From Figure S8d–f (Supporting Information), as predicted by DFT, Ga generally displays a higher binding energy to graphene than Ag when placed above or below the bilayer graphene with these three types of vacancies. For the larger trideca-vacancy, the binding energy differences between Ag and Ga above the bilayer graphene are not as pronounced when compared to the smaller vacancy size. On the other hand, with mono- or trideca-vacancies present, Ga ex-

hibits a slightly lower binding energy to graphene than Ag when placed between the bilayers of graphene. This provides insight where there may be additional resistance for Ga atoms to initially de-intercalate from under the bilayer graphene. However, once the Ga atoms are located between the graphene layers, the de-intercalation kinetics becomes much faster and Ga atoms readily move to the top graphene surface. All the DFT and ReaxFF calculated binding energies for Ag and Ga to defective graphene are stated in Table S4 (Supporting Information).

When considering pristine bilayer graphene, it becomes evident that an isolated Ga atom also exhibits higher binding energies than an isolated Ag atom. The binding energies were calculated when the metal atom is initially placed at different adsorption sites (i.e., above, below, and between graphene layers with respect to either a vertex (location 1) or the center (location 2) of a hexagonal ring in graphene lattice) on the graphene, as illustrated in Figure S18m (Supporting Information). The observation suggests that, in comparison with Ag, Ga can more stably bind with pristine graphene, both on the top and underneath the bilayer graphene, making it less likely to re-intercalate once it is on top of the graphene surface. The intercalation of Ag and Ga atoms between pristine bilayer graphene results in positive binding energies. For Ag cases, this is accompanied by a notable distortion of the top graphene lattice, as seen in Figure S18e,f (Supporting Information). Conversely, Ga cases exhibit a slight displacement of the top graphene lattice, as depicted in Figure S18g,h (Supporting Information). These effects could introduce deformation energy into the system, resulting in binding energies of 130.22 and 128.02 kcal mol<sup>-1</sup> for Ag at locations 1 and 2, respectively. Similarly, binding energies of 59.02 and 46.27 kcal mol<sup>-1</sup> are observed for Ga at locations 1 and 2, respectively.

Figure S19s (Supporting Information) reveals slightly distinct behaviors, where 1-, 2-, and 3-layer Ag and Ga are positioned at

various adsorption sites (i.e., above, below, and between graphene layers). Layered Ga cases always exhibit higher binding energies in comparison to their layered Ag counterparts, regardless of the selected adsorption sites. Moreover, Ag and Ga have a stronger binding strength between bottom layer graphene and SiC substrate than the other adsorption sites, regardless of the number of metal layers. This observation suggests a stronger interaction with the bilayer graphene and SiC surface for layered Ga. As a result, despite the notably lower melting point of Ga compared to that of Ag, fluid-like Ga atoms can stably reside beneath the bilayer graphene during high temperature annealing, thus serving as a stable source for Ga accumulation and piling up between the graphene layers.

The results from both DFT and ReaxFF calculations suggest that the chemisorption of de-intercalated Ga atoms onto the defective graphene surface can hinder and prevent Ga re-intercalation, which is consistent with the PEEM-based experimental results shown in Figure 3. In contrast, the physisorption of de-intercalated Ag atoms to defective graphene suggests that the Ag atoms could be more mobile and enabling the Ag atoms to re-intercalate, consistent with the experimental results (see Figure 2). Similar calculated observations were made in other metal-graphene intercalation systems, where the authors found the intercalation process is limited by the metal-metal detachment at vacancies prior to intercalation.<sup>[34]</sup>

To reveal the de- and re-intercalation atomistic mechanisms of metal atoms through defective graphene, we perform annealing MD simulations for the Gr/Ag/SiC and Gr/Ga/SiC systems while varying the temperature, size, and density of defects. The ratios of de-intercalated to intercalated metal atoms are evaluated in Figure 5a–d as they move between the bilayer graphene or through the top layer graphene with the four types of vacancies. In all of these scenarios, the ratio of de-intercalated Ga is significant. As the effective size of the vacancy becomes larger, the proportion of Ga between graphene layers increases at lower annealing temperatures (Figure 5b–d). At 2500 K, a small number of de-intercalated Ga atoms emerge to the top graphene layer. From Figure 5a–c, for the systems with only one vacancy on each graphene layer, the ratio of de-intercalated Ag atoms is negligible compared with that of de-intercalated Ga atoms. As the number of tetra-vacancies increases (Figure 5d), de-intercalated Ag becomes noticeable between the layers of graphene. The different clustering pattern of de-intercalated Ag and Ga atoms between and above the bilayer graphene with a trideca-vacancy on each graphene layer are presented as VMD snapshots at different temperatures in Figure 5e–j. At 300 K (Figure 5e,h, both Ag and Ga systems have no metal de-intercalation, while buckling of graphene can be observed in the Ga system due to the concentrated local stress caused by the phase transition of Ga.<sup>[35]</sup> At 1500 K, a 2D cluster of Ga atoms forms between the bilayer graphene (Figure 5i), and then the Ga atoms de-intercalate to the top layer graphene as the temperature is raised to 2500 K (Figure 5j). In contrast, there is no buildup of Ag between the layers of graphene (Figure S13f–j, Supporting Information). At 2000 K and higher, de-intercalated Ag atoms diffuse to the top graphene surface, however, at a much smaller proportion of atoms compared to the Ga system. For the Ga-containing system at 2500 K, the presence of a single type of defect in graphene causes thermal decomposition and rupture of bilayer graphene,

leading to the formation of larger defects or even cracks that enable a larger density of Ga atoms to escape to the top graphene surface (see Figures S9o, S10o, and S11o, Supporting Information). For the Ag-containing system, both the intercalated Ag and the bilayer graphene can maintain its initial crystallinity and structure at 2500 K (see Figures S9e, S10e, and S11e, Supporting Information).

The effects of heterostructures with respect to the layer numbers of intercalated metals and graphene are also examined using ReaxFF MD simulations. In Figure S17 (Supporting Information), the Gr/metal/SiC systems, comprising 1-, 2-, 3-, and 4-layer Ag and Ga beneath bilayer graphene, as well as 3-layer Ag and Ga beneath mono- or bilayer graphene, are subjected to an annealing at 1000 K for 0.5 ns. A single trideca vacancy is introduced either within the monolayer graphene or within each layer of bilayer graphene. As depicted in Figure S17f–i (Supporting Information), Ag atoms maintain their layered structures, and only a few Ag atoms escape to the top layer graphene, with no significant buildup observed. In contrast, in the Ga cases shown in Figure S17p–s (Supporting Information), Ga atoms melt and disperse uniformly over the space between the bilayer graphene and the SiC substrate. As the number of Ga layers increases to 2, two layers of Ga consistently remain between the bilayer graphene and the SiC substrate, while excess Ga atoms migrate upward, traversing vacancies to reach the top layer of graphene. The size of Ga accumulation between the bilayer graphene increases as the number of Ga layers is raised, as observed from the top views of the Gr/Ga/SiC systems in Figure S17l–n (Supporting Information). Comparing Figure S17e,j (Supporting Information) with Figure S17c,h (Supporting Information), it is evident that 3-layer Ag remains positioned between the graphene layer and the SiC substrate, maintaining its initial crystallinity. On the other hand, in the comparison of Figure S17o,t (Supporting Information) with Figure S17m,r (Supporting Information), only two layers of Ga can be sustained between the graphene layer and the SiC substrate. Meanwhile, another portion of Ga atoms either intercalates between the bilayer graphene layers or migrates to the top surface of the monolayer graphene. These results suggest that the thermophysical properties of the metal intercalant and/or intercalant-graphene interactions play an influential role in the de-intercalation kinetics as observed in the experimental results, and heterostructures of graphene or metal intercalants have minimal impacts on these behaviors. As shown in Figure 3b, the Ga de-intercalation exhibits an abrupt transition with varying delayed onset. Based on ReaxFF MD results, we propose that this abrupt transition is due to the Ga piling up between the graphene layers (delayed onset) and then graphene bursting (abrupt transition). On the other hand, the Ag de- and re-intercalation displayed slower kinetics and apparent linear diffusion in the experiment, consistent with ReaxFF MD where intercalated Ag atoms simply move through graphene defects to arrive to the top graphene surface.

The quasi-reversibility of de- and re-intercalation observed in the Ag system is also supported by atomistic simulations. Taking the trideca-vacancy system annealed at 2000 K as an example (Figure S16, Supporting Information), at time instants from 0.25 ns to 2.00 ns, the number of Ag atoms emerging between or on the top of bilayer graphene alternately decreases and increases during the annealing process. In contrast, the number of

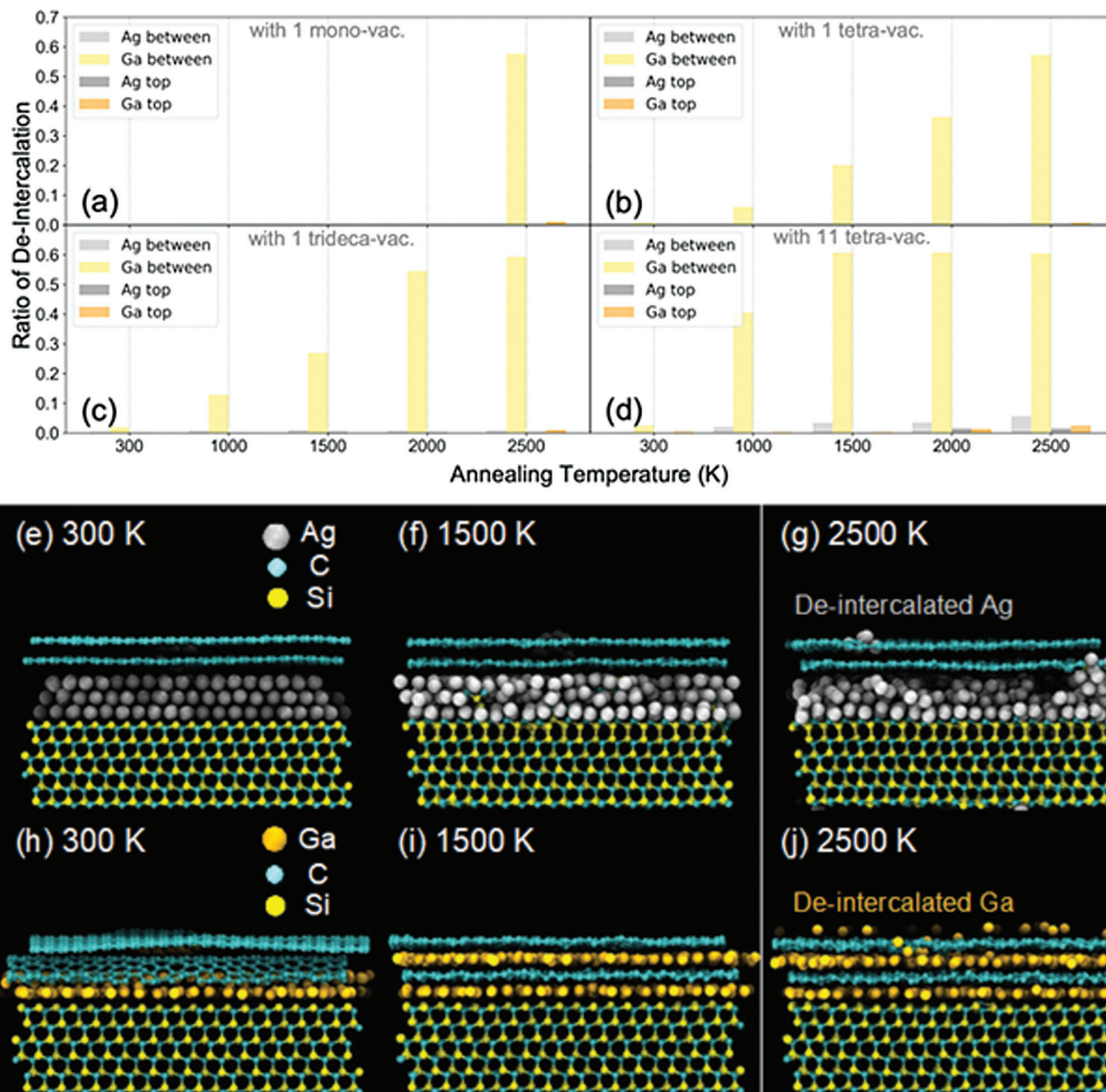


**Figure 5.** De-intercalation of Ag and Ga atoms during annealing at elevated temperatures from ReaxFF MD simulations. Ratios of de-intercalated Ag and Ga atoms located between and on top of bilayer graphene with a) 1 mono-vacancy, b) 1 tetra-vacancy, c) 1 trideca-vacancy, and d) 11 tetra-vacancies on each layer of graphene annealed at 300, 1000, 1500, 2000, and 2500 K for 0.5 ns. Snapshots showing the metal atom de-intercalation details for e–g) Ag and h–j) Ga CHet systems annealed at 300, 1500, and 2500 K for 2.00 ns, where 1 trideca-vacancy is included in each graphene layer.

Ga atoms between or on the top layer of bilayer graphene only continues to increase.

The intercalation dynamics is influenced by the thermophysical properties of the intercalant. The in situ annealing is performed at a maximum temperature of 622 K, indicating the presence of liquid Ga, which promotes Ga removal from the sample. The de-intercalation of cesium at the graphene-iridium interface was observed at temperatures greater than 773 K and occurred rapidly,<sup>[21]</sup> similar to the observation here with 2D Ga. The melting point of cesium is 301 K,<sup>[35]</sup> nearly identical to Ga, which supports that the de-intercalation dynamics is influenced by the liq-

uid metal intercalant. When the temperature surpasses the melting temperature of the metal intercalant, the surface tension and viscosity of the liquid metal decreases<sup>[36]</sup> due to the increase of molecular thermal activity. At 622 K, the viscosity of liquid Ga will have decreased to at least half of its value when compared to its value at the melting point (302 K).<sup>[36]</sup> In response to the changing properties of liquid Ga, the defective regions of graphene (or intercalation windows) expanded, which was observed as the tiling or bursting seen in the PEEM results.

These intercalation simulations clearly support the experimentally observed faster kinetics characteristic for Ga atoms,

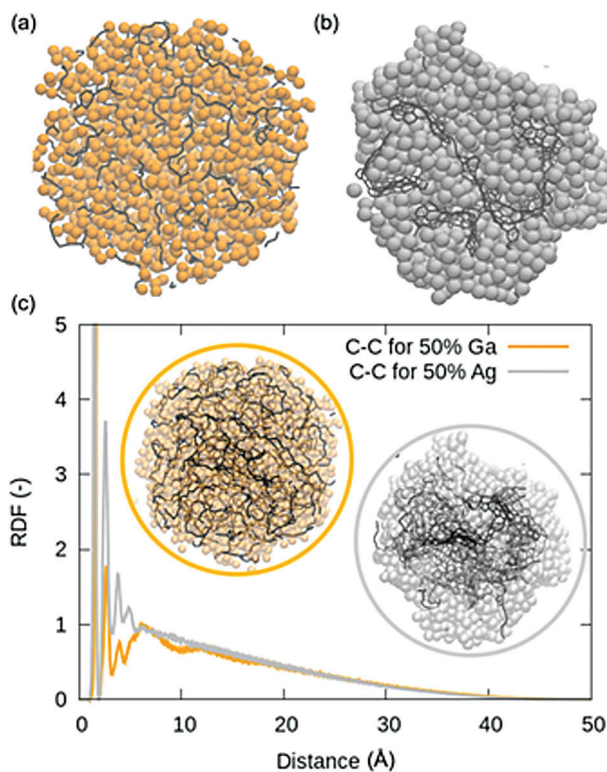


**Figure 6.** Segregation of Ga and Ag atoms from C-containing droplets during annealing process from ReaxFF MD simulations. Cross-sectional views of molecular structures of a) Ga-C droplet, b) Ag-C droplet annealed at 2800 K for 0.50 ns, and c) C–C pairwise pair radial distribution function (RDF) plots for Ga-C and Ag-C systems with a metal:C mixing atomic ratio of 1:1 are presented in sequence.

resulting from intrinsic differences in the interactions between the different metals and carbon. These differences in the metal-carbon interactions can also influence metal-carbon segregation dynamics. The presence of Ag could potentially expedite the healing process of graphene defects, while the presence of Ga could stabilize or even enlarge these defects. To investigate these potential differences in the metal-carbon segregation dynamics, two droplet models consisting of Ga-C and Ag-C are considered. The cross-sectional views of the final configuration for both Ga-C and Ag-C droplets are presented in **Figure 6a,b**, where the metal atoms are represented as spheres (in orange for Ga, gray for Ag) and all carbon-carbon bonds are represented as the black sticks. There is a significant difference in the carbon-carbon bond distribution characteristic for each of these models: more concentrated and interconnected for the Ag-C system compared to more dispersed for the Ga-C droplet. To quantify these differences, we compare the pair radial distribution function (RDF) for all carbon atoms, as shown in **Figure 6c**. There are much more pronounced peaks for the system with 50% Ag atoms (in gray) compared to the system with 50% Ga atoms (in orange). These pronounced peaks are present not only for the characteristic distance of the C–C bond ( $<2$  Å and discussed in more details in the Supporting Information), but also for longer distances (up to 10 Å). The difference in the carbon-carbon network characteristic for the Ag- and Ga-based droplets is highlighted in **Figure 6c** in-

sets. The pronounced RDF peaks in the Ag-C system is indicative of faster Ag-C segregation dynamics, resulting from a relatively weaker metal-C interaction, and leading to an evolution of the extended carbon-carbon network of six-membered carbon ring specific for an early stage of a graphitization process. Conversely, this suggests that Ga-C interaction is stronger than the Ag-C, with propensity to intermix. This implies that Ag can assist in graphene healing while, in contrast, Ga can increase the defect size in graphene. This is supported by the experimental observation of the de-intercalated metal height distribution. The Ag-containing clusters on the surface after de-intercalation tended to be 10–20 nm tall (see **Figure S3d**, Supporting Information), while the Ga-containing clusters were  $\approx 100$  nm tall (see **Figure 7d**).

While the interactions between metal intercalants and defective graphene during intercalation is now understood, we turn our attention to understanding the origin of the different appearances of the intercalation “windows” (or defects) in both the 2D Ag and Ga system. To identify the origin of the dynamic, distinctly-shaped features observed during Ga de-intercalation, we conduct ex situ AFM, KPFM, and SEM-EDX measurements after the in situ annealing PEEM studies. Similar triangular features to those seen in the PEEM images (bright features like ROI 1 in **Figure 3**) are observed with SEM (**Figure 7a**, dashed red line) and confocal optical imaging (not shown). Lines of clustered Ga are also present and confirmed by SEM-EDX (**Figure S6**, Supporting Information), and similar clusters are observed in AFM measurements, as shown in **Figure 7d**, which indicate that these Ga clusters are located on top of the graphene. These lines of Ga clusters are also observed in samples that did not undergo the in situ annealing PEEM and have been observed in other instances,<sup>[4]</sup> and are likely formed as a result of the initial CHet process. The area of the same triangular feature seen by SEM (**Figure 7a**) are located by AFM topography and KPFM CPD mapping, as depicted in **Figure 7b,c**, respectively. The triangular feature itself is not visible in the AFM topography map, indicating that the contrast observed with PEEM (and SEM) is not of topographic origin. However, while using the KPFM mode, the region where the triangular feature is expected coincides with a region of higher CPD when compared to its surroundings (**Figure 7c**). We find that  $\approx 47\%$  of all pixels in the triangular region exhibit a potential greater than 5 mV. The higher potential indicates a change in the electronic structure of the triangular feature compared to its surroundings. The increase in surface potential, as shown in **Figure 7c**, could indicate the presence of intercalated gallium,<sup>[4]</sup> defective graphene,<sup>[37]</sup> or defective graphite.<sup>[38]</sup>

These triangular features are also observed by PEEM (**Figure 7e**) and SEM on Gr/SiC with and without plasma treatment of the CHet process. Similar triangular and elongated motifs have been observed in SiC wafers and homoepitaxy of SiC, and they originate from basal plane dislocations, threading edge dislocations, and stacking faults from the SiC crystal.<sup>[39,40]</sup> These crystallographic defects can extend and propagate to epitaxial films and create surface defects.<sup>[39]</sup> Based on the 2D Ga de-intercalation, we propose that the bright, distinctly-shaped features are highly defective regions of graphene that are extended defects from underlying SiC and serve as windows that allow the metal to exit from the Gr/SiC interface during the deintercalation process.

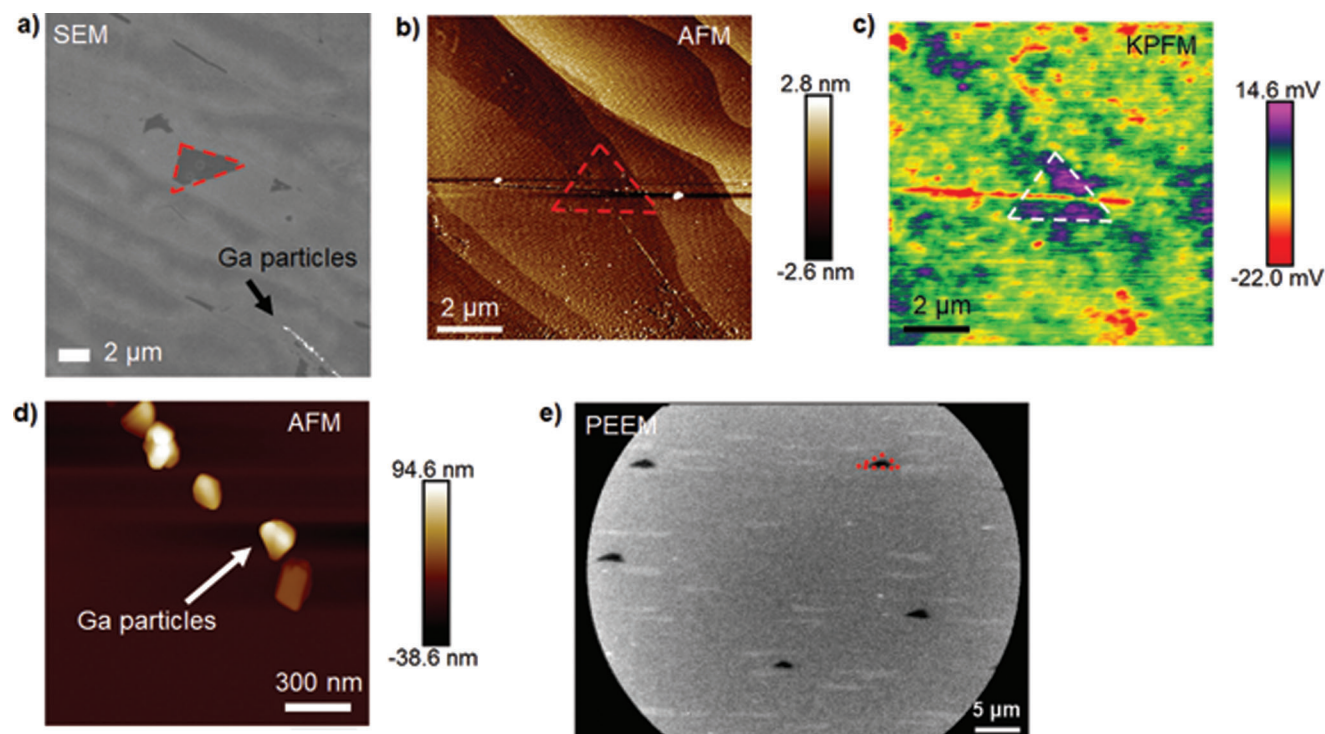


**Figure 7.** Topographic features in the in situ annealed Gr/Ga/SiC sample as seen in complementary imaging techniques. In (a), SEM micrograph of a triangular feature (marked with dashed red line) that is similar to ROI in Figure 3 and presence of Ga particles identified by EDX (Figure S6, Supporting Information). The same feature in (a) is identified in b) AFM topography and c) KPFM CPD images (dashed line as a guide to the eye). The Ga particles are above the sample surface in d) AFM topographic image and is the same region identified in (a). In (e), PEEM image of an oxygen plasma treated Gr/SiC sample with one proposed defective region marked in red dash line.

While the CHet intercalation process heals some graphene defects,<sup>[3]</sup> different intercalants are expected to interact with graphene defects in dissimilar ways. The intercalation of Ga through defective graphene was computationally studied, and the size of the defect, as well as the local bonding to the Ga atom, is proposed to influence the intercalation energetics.<sup>[25]</sup> The de-intercalation velocity front of hydrogen spatially varied over two orders of magnitude, suggesting its dependence on the nature of graphene defects.<sup>[20]</sup> Those results<sup>[20,25]</sup> and our observations imply that the specific intercalant and its interaction with graphene defects affect the intercalation dynamics; here, the generation of defects by plasma is nominally identical in the CHet process. Thus, we propose that the 2D Ag CHet heals the graphene defects much more effectively than 2D Ga CHet that is supported by the observation of intercalation windows appearing smaller and circular in shape (as illustrated in **Figure 8**).

### 3. Conclusion

We successfully tracked the de-intercalation of two different systems, namely, 2D Ag and 2D Ga, from the graphene-SiC interface, which provided insight into the intercalation mechanism. These processes were observed in real time via in situ annealing with photoemission electron microscopy (PEEM), with thermodynamic insights to the processes provided by DFT calculations and ReaxFF MD simulations. The 2D Ag is unique in that both de- and re-intercalation are observed through circular intercala-

tion windows (defect). We find that the 2D Ag intercalation velocity front is  $0.5 \text{ nm s}^{-1} \pm 0.2 \text{ nm s}^{-1}$ . In contrast, the 2D Ga results in irreversible de-intercalation with considerably faster kinetics dependent on the defect shape. ReaxFF MD captured the Ag atoms moving through graphene to de- and re-intercalate; it also predicted a more complex phenomena of Ga atoms first

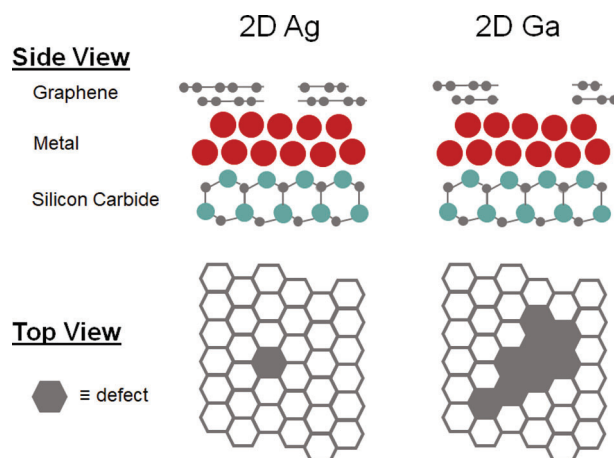


**Figure 8.** Proposed scheme of 2D metal intercalation and its interaction with defects in graphene. The intercalation of 2D Ag heals the defects more effectively than the 2D Ga system.

accumulating between the graphene bilayer before ultimately diffusing to the top graphene surface. The defects or intercalation windows manifest in very different shapes in the 2D Ag and 2D Ga systems, which we propose originates from different defective graphene healing mechanisms in response to the metal-defective graphene intercalations. These ReaxFF results are confirmed by DFT calculations that indicate that the physisorption of Ag to a plasma-treated graphene can lead to the re- and de-intercalation of Ag through graphene. While in contrast, Ga atoms covalently interact with the surface, suggesting that once Ga atoms de-intercalate from the interface, they stick to the graphene surface, preventing the re-intercalation of Ga atoms at the interface. This combined theoretical and experimental work provides a new insight on the role of defect formation, healing, and interaction with metal intercalants in the intercalation dynamics in 2D materials.

#### 4. Experimental Section

**Experimental Methods:** The intercalated silver (Gr/Ag/SiC) and gallium (Gr/Ga/SiC) epitaxial graphene samples were prepared as reported by the CHet process.<sup>[3]</sup> Monolayer epitaxial graphene (EG) was formed via annealing 6H-SiC substrates at 1800 °C (2073.15 K) for 20 min in pure argon. Then EG was treated by oxygen plasma in a Tepla M4L plasma etch tool,<sup>[41]</sup> with 150 sccm O<sub>2</sub> and 50 sccm He under a pressure of 50 mTorr (6.67 Pa) and a power of 50 mW for 60 s. Gr/Ag/SiC and Gr/Ga/SiC samples were prepared via annealing O<sub>2</sub> plasma treated EG and metallic precursors at high temperature of 950 °C (1223.15 K) and 800 °C (1073.15 K) for Ag and Ga intercalation, respectively. The intercalation process detaches the buffer layer from SiC and becomes EG, which overall results in a bilayer EG metal-intercalated system.<sup>[4]</sup>

The samples were vacuum sealed at The Pennsylvania State University and sent to NIST, where they were kept sealed in vacuum or inert gas atmospheres except during sample transfer into the vacuum chamber. The PEEM at NIST was manufactured by a commercial vendor<sup>[42,43]</sup> and the data acquisition and correction were described previously.<sup>[44]</sup> In situ heating capabilities in the PEEM were performed in the temperature range of 293 to 622 K, and all measurements were done with a non-monochromatic mercury arc source with a 15 kV acceleration voltage, and ultrahigh vacuum (UHV) with an initial base pressure of  $5 \times 10^{-10}$  mbar (or  $5 \times 10^{-8}$  Pa). The uncertainty of the temperature reading was  $\approx 4\%$  due to the contact between the sample surface and thermocouple junction on the sample holder. The PEEM images of the in situ measurements were taken with an exposure time of 500 ms per image and three sequential images were averaged to make an image frame. Each frame was recorded every 1 and 0.5 min for the Gr/Ag/SiC and Gr/Ga/SiC measurements, respectively. Difference images were determined as,  $\text{difference}[t] = \text{image}[t] - \text{image}[t_0]$ , where  $t_0$  was  $t = 0$  min during a particular in situ annealing cycle. After PEEM measurements were completed, the samples were analyzed by atomic and Kelvin probe force microscopy (AFM and KPFM), scanning electron microscopy (SEM), energy dispersive X-ray spectroscopy (EDX) and X-ray photoelectron spectroscopy (XPS). A commercial tapping-mode AFM and KPFM in air was used to compare the topographic and contact potential difference (CPD) results with the PEEM. EDX-SEM and XPS were used to verify the chemical nature of the topographic features and the presence of intercalated Ag and Ga in each sample before and after in situ PEEM measurements and results were consistent with earlier CHet characterization results<sup>[3,25]</sup> and from other fabrication procedures.<sup>[45]</sup> The XPS used here had an analytical area of  $\approx 1$  mm<sup>2</sup> utilizing a monochromated Al K $\alpha$  photon source with a hemispherical electron analyzer pass energy of 20 eV.

**Computational Methods:** Gr/Ag/SiC and Gr/Ga/SiC systems were investigated using DFT and ReaxFF molecular dynamics (MD) method. The

detailed description for both methods are provided in the Supporting Information and summarized in the following subsections.

**DFT Calculations for Binding Energies of Ag and Ga to Defective Graphene:** DFT calculations were performed with the Quantum Espresso package<sup>[41,46]</sup> using the projected augmented potential<sup>[47,48]</sup> within the generalized gradient approximation functional of Perdew, Burke, and Ernzerhof.<sup>[49,50]</sup> A  $5 \times 5 \times 1$   $\Gamma$ -centered Monkhorst-Pack k-point mesh was used to sample Brillouin Zone with a kinetic energy cut-off of 60 Ry and a density cutoff of 600 Ry. All systems were relaxed to their ground states using a Broyden-Fletcher-Goldfarb-Shanno algorithm. Thresholds for the total energy and force were set to 0.0001 Ry and 0.001 Ry  $\text{\AA}^{-1}$ , respectively. Periodic boundary conditions were imposed along the three directions of the space with a vacuum layer of 20  $\text{\AA}$  along the out-of-plane direction of graphene. We considered a  $6 \times 6 \times 1$  hexagonal supercell of a pristine graphene with the dimensions of 1.476 nm  $\times$  1.476 nm  $\times$  2.0 nm to construct four representative defect models with single (SV), double (DV), hepta- (7 V) and octa- (8 V) vacancies. The undercoordinated C atoms of SV and 7 V models were functionalized with hydroxyl (COH) and carbonyl (CO =) functional groups while only the epoxy group (COC) was considered for the functionalization of the DV and 8 V models.

**ReaxFF:** ReaxFF was a bond order potential allowing for modeling complex chemical environments such as chemical vapor deposited growth of 2D materials by allowing bond breaking and reformation during the simulations. Here, taking the original Ga/C/H and Si/C/H parameters from the previous work,<sup>[25,51–53]</sup> a new ReaxFF Ag/Ga/Si/C/H/O-2023 force field was developed to model Ag and Ga interactions with graphene defects in a CHet process, thus, to mimic experimentally observed the de- and re-intercalation mechanisms for Ag and Ga atoms. It was worth mentioning that the force field devised by Nayir et al.<sup>[25]</sup> specifically focuses on Ga interactions exclusively with O-functional group-absent free-standing graphene and does not consider graphene/Ag interactions. In contrast, the force field presented in this study enables to model both Ga and Ag intercalation within SiC/O-functionalized graphene, more closely resembling experimental conditions. The details of the force field parameterization are given in the Supporting Information along with the force field parameter set. All MD simulations were performed with the Amsterdam Modeling Suite (AMS),<sup>[54]</sup> and the simulation snapshots were generated with use of the Visual Molecular Dynamics (VMD),<sup>[55]</sup> the (Open Visualization Tool) OVITO<sup>[56]</sup> and VESTA<sup>[57]</sup> software.

To understand the re-/de-intercalation mechanisms of Ag and Ga atoms at the SiC/graphene interface, MD simulations were performed using the newly developed ReaxFF Ag/Ga/Si/C/H/O-2023 force field. Note that thermodynamic and kinetic preferences of a metal atom's behavior, particularly in relation to its adsorption on graphene, bilayer arrangement, or intercalation into the SiC/graphene gallery, were influenced by interactions among intercalants, defects, graphene, and SiC. Prior investigations have provided comprehensive insights into this phenomenon.<sup>[3,25,26,58–60]</sup> Gallium (Ga) tends to favor intercalation via the multivacancy defect (>divacancy) over mere adsorption atop the graphene layer and this intercalation process was notably barrier-free.<sup>[25,26]</sup> This indicates that Ga intercalation into the SiC/graphene gallery was kinetically favorable. From the thermodynamic aspect, the presence of the SiC substrate beneath the graphene layer introduces thermodynamic asymmetry on the potential energy surface, causing a lower local energy minimum compared to the adsorption atop of graphene layer. As a consequence, Ga exhibits a thermodynamic preference to stay at the SiC/graphene interface<sup>[26]</sup> and this phenomenon has also been observed for various metals.<sup>[58–60]</sup> From this point forward, three layers of Ag and Ga, containing 756 atoms, were separately sandwiched between an AB-stacked bilayer graphene and (0001) SiC substrate in a 53.59  $\text{\AA} \times 61.88 \text{\AA} \times 100 \text{\AA}$  orthogonal simulation box. The primary reason of choosing three layers of metal at the heterointerface was rooted in the observations made by scanning transmission electron microscopy and theoretical calculations of 3 atomic layers of Ga.<sup>[3]</sup> In addition, the simulated annealing trial tests carried out at high temperatures (above 1000 K) for 1-, 2-, 3-, and 4-layer Ga confirm the efficacy of adopting a three-layer metal configuration for this study. The study observed that the Ga layers melted and diffused uniformly across the spacing between the defective bilayer graphene and the SiC substrate.

When the number of Ga layers reached 2, two layers of Ga consistently remained between the bilayer graphene and SiC substrate, with the excess Ga atoms moving upward and traveling through vacancies to reach the top layer graphene, as can be seen in Figure S17q–s (Supporting Information). As such, the use of 3-layer Ga configuration provides a reasonable setup, allowing for the observation of diffusion both beneath and on top of the defective bilayer graphene in our ReaxFF MD simulations. Similarly, this identical layer configuration was employed for the Ag layer to uphold consistency in the calculations. A vacuum of 78.31 Å was inserted along z direction to avoid the spurious interactions between replicas. In addition, four defect models were adopted for each Ag and Ga systems by introducing one mono-, tetra-, trideca-, and eleven tetra-vacancies in both layers of graphene. Upon the structural relaxation of the eight models using the conjugate gradient method, each system was annealed at 300, 1000, 1500, 2000, and 2500 K with a time step of 0.25 ns for 0.5 ns in an NVT ensemble, where the temperature fluctuations were controlled using the Berendsen thermostat with a temperature damping parameter of 100 fs. It is noteworthy that elevated temperatures such as 1500 K were used to expedite the reaction kinetics, enabling the intercalation mechanisms to be assessed within a nanosecond timescale. For the systems with trideca- and eleven tetra-vacancies, the annealing time was extended to 2.0 ns, with an aim to tracing the re- and de-intercalation of both Ag and Ga.

To assess the comparative metal-carbon segregation dynamics of Ag and Ga, the MD annealing simulations of amorphous metal-carbon droplets were performed. The study considered two droplet models consisting of 2000 metal atoms, Ga or Ag, and 2000 carbon atoms, where all atoms were initially placed randomly in box: 100 Å × 100 Å × 100 Å. After the minimization and the box deformation to the density equal an average of the density characteristic for the amorphous carbon (2.3 g cm<sup>-3</sup>) and metal (10.5 g cm<sup>-3</sup> for Ag and 5.1 g cm<sup>-3</sup> for Ga), the droplets were suspended in a vacuum (placed in the center of the box: 300 Å × 300 Å × 300 Å). These initial structures were 1) equilibrated at 300 K for 0.5 ns, 2) heated from 300 to 2800 K with a rate of 5 K ps<sup>-1</sup> and 3) annealed at 2800 K for another 0.5 ns. All droplet simulations were performed at constant volume, with use of NVT ensemble, time step: 0.25 fs and the Berendsen thermostat with a temperature damping parameter of 100 fs.

## Supporting Information

Supporting Information is available from the Wiley Online Library or from the author.

## Acknowledgements

F.N. acknowledges support from the PREP UMD – NIST program (grant number 70NANB18H165). A.W. acknowledges support from the PREP Georgetown – NIST program (grant number 70NANB18H161). Samples for this publication were provided by The Pennsylvania State University 2D Crystal Consortium – Materials Innovation Platform (2DCC-MIP), which was supported by the NSF cooperative agreement DMR-1539916NSF 2D CC. The authors thank the NIST Center for Nanoscale Science and Technology for SEM-EDX support. The authors thank Henry G. Bell for aiding in code developed to analyze the PEEM data. Q.M., N.N., M.K., and A.D. acknowledge the funding from the National Science Foundation 2D Crystal Consortium – Materials Innovation Platform (NSF 2DCC-MIP) under cooperative agreement DMR-1539916. Computations for this research were performed on the PSU's Institute for Cyber Science Advanced Cyber Infrastructure (ICS-ACI).

## Conflict of Interest

The authors declare no conflict of interest.

## Data Availability Statement

The data that support the findings of this study are available from the corresponding author upon reasonable request.

## Keywords

defects, dynamics, graphene, intercalation, molecular dynamics, photoemission electron microscopy

Received: September 8, 2023

Revised: October 6, 2023

Published online: November 2, 2023

- [1] P. V. Pham, S. C. Bodepudi, K. Shehzad, Y. Liu, Y. Xu, B. Yu, X. Duan, *Chem. Rev.* **2022**, *122*, 6514.
- [2] N. Briggs, Z. M. Gebeyehu, A. Vera, T. Zhao, K. Wang, A. De La Fuente Duran, B. Bersch, T. Bowen, K. L. Knappenberger, J. A. Robinson, *Nanoscale* **2019**, *11*, 15440.
- [3] N. Briggs, B. Bersch, Y. Wang, J. Jiang, R. J. Koch, N. Nayir, K. Wang, M. Kolmer, W. Ko, A. De La Fuente Duran, S. Subramanian, C. Dong, J. Shallenberger, M. Fu, Q. Zou, Y.-W. Chuang, Z. Gai, A.-P. Li, A. Bostwick, C. Jozwiak, C.-Z. Chang, E. Rotenberg, J. Zhu, A. C. T. van Duin, V. Crespi, J. A. Robinson, *Nat. Mater.* **2020**, *19*, 637.
- [4] H. El-Sherif, N. Briggs, B. Bersch, M. Pan, M. Hamidinejad, S. Rajabpour, T. Filleter, K. W. Kim, J. Robinson, N. D. Bassim, *ACS Appl. Mater. Interfaces* **2021**, *13*, 55428.
- [5] C. Berger, Z. Song, T. Li, X. Li, A. Y. Ogbazghi, R. Feng, Z. Dai, A. N. Marchenkov, E. H. Conrad, P. N. First, W. A. De Heer, *J. Phys. Chem.* **2004**, *108*, 19912.
- [6] C. Riedl, C. Coletti, U. Starke, *J. Phys. D: Appl. Phys.* **2010**, *43*, 374009.
- [7] S. Wu, Q. Zhang, H. Yang, Y. Ma, T. Zhang, L. Liu, H.-J. Gao, Y. Wang, *Prog. Surf. Sci.* **2021**, *96*, 100637.
- [8] M. S. Stark, K. L. Kuntz, S. J. Martens, S. C. Warren, *Adv. Mater.* **2019**, *31*, 1808213.
- [9] M. Laipan, L. Xiang, J. Yu, B. R. Martin, R. Zhu, J. Zhu, H. He, A. Clearfield, L. Sun, *Prog. Mater. Sci.* **2020**, *109*, 100631.
- [10] L. Daukiya, M. N. Nair, M. Cranney, F. Vonau, S. Hajjar-Garreau, D. Aubel, L. Simon, *Prog. Surf. Sci.* **2019**, *94*, 1.
- [11] J. Wan, S. D. Lacey, J. Dai, W. Bao, M. S. Fuhrer, L. Hu, *Chem. Soc. Rev.* **2016**, *45*, 6742.
- [12] K. H. Kim, H. He, C. Struzzi, A. Zakharov, C. E. Giusca, A. Tzalenchuk, Y. W. Park, R. Yakimova, S. Kubatkin, S. Lara-Avila, *Phys. Rev. B* **2020**, *102*, 165403.
- [13] L. Jin, Q. Fu, R. Mu, D. Tan, X. Bao, *Phys. Chem. Chem. Phys.* **2011**, *13*, 16655.
- [14] Y. Cui, J. Gao, L. Jin, J. Zhao, D. Tan, Q. Fu, X. Bao, *Nano Res.* **2012**, *5*, 352.
- [15] L. Jin, Q. Fu, Y. Yang, X. Bao, *Surf. Sci.* **2013**, *617*, 81.
- [16] C. Virojanadara, A. A. Zakharov, S. Watcharinyanon, R. Yakimova, L. I. Johansson, *New J. Phys.* **2010**, *12*, 125015.
- [17] C. Xia, S. Watcharinyanon, A. A. Zakharov, R. Yakimova, L. Hultman, L. I. Johansson, C. Virojanadara, *Phys. Rev. B* **2012**, *85*, 045418.
- [18] C. Xia, S. Watcharinyanon, A. A. Zakharov, L. I. Johansson, R. Yakimova, C. Virojanadara, *Surf. Sci.* **2013**, *613*, 88.
- [19] K. V. Emtsev, A. A. Zakharov, C. Coletti, S. Forti, U. Starke, *Phys. Rev. B* **2011**, *84*, 125423.
- [20] T. A. De Jong, E. E. Krasovskii, C. Ott, R. M. Tromp, S. J. Van Der Molen, J. Jobst, *Phys. Rev. Mater.* **2018**, *2*, 104005.
- [21] M. Petrovic, I. Srut Rakic, S. Runte, C. Busse, J. T. Sadowski, P. Lazic, I. Pletikovic, Z.-H. Pan, M. Milun, P. Pervan, N. Atodiresi, R. Brako, D. Sokcevic, T. Valla, T. Michely, M. Kralj, *Nat. Commun.* **2013**, *4*, 2772.
- [22] A. Stöhr, S. Forti, S. Link, A. A. Zakharov, K. Kern, U. Starke, H. M. Benia, *Phys. Rev. B* **2016**, *94*, 085431.
- [23] S. Schumacher, F. Huttman, M. Petrovic, C. Witt, D. F. Förster, C. VoVan, J. Coraux, A. J. Martínez-Galera, V. Sessi, I. Vergara, R. Rückamp,

- M. Grüninger, N. Schleheck, F. Meyer Zu Heringdorf, P. Ohresser, M. Kralj, T. O. Wehling, T. Michely, *Phys. Rev. B* **2014**, *90*, 235437.
- [24] Z. Y. Al Balushi, K. Wang, R. K. Ghosh, R. A. Vilá, S. M. Eichfeld, J. D. Caldwell, X. Qin, Y.-C. Lin, P. A. Desario, G. Stone, S. Subramanian, D. F. Paul, R. M. Wallace, S. Datta, J. M. Redwing, J. A. Robinson, *Nat. Mater.* **2016**, *15*, 1166.
- [25] N. Nayir, M. Y. Sengul, A. L. Costine, P. Reinke, S. Rajabpour, A. Bansal, A. Kozhakhmetov, J. Robinson, J. M. Redwing, A. Van Duin, *Carbon* **2022**, *190*, 276.
- [26] N. Nayir, *J. Mater. Res.* **2022**, *37*, 1172.
- [27] X. Jiang, B. Song, D. Tománek, *Phys. Rev. Appl.* **2018**, *9*, 044015.
- [28] Z. Osváth, A. Deák, K. Kertész, G. Molnár, G. Vértesy, D. Zámbo, C. Hwang, L. P. Biró, *Nanoscale* **2015**, *7*, 5503.
- [29] P. L. Houston, *Chemical Kinetics and Reaction Dynamics*, Dover Publications, Garden City, NY, **2006**.
- [30] J. Robinson, X. Weng, K. Trumbull, R. Cavaleiro, M. Wetherington, E. Frantz, M. Labella, Z. Hughes, M. Fanton, D. Snyder, *ACS Nano* **2010**, *4*, 153.
- [31] Y. Gan, L. Sun, F. Banhart, *Small* **2008**, *4*, 587.
- [32] J. C. Kotsakidis, M. Currie, A. Grubisic-Cabo, A. Tadich, R. L. Myers-Ward, M. Dejarld, K. M. Daniels, C. Liu, M. T. Edmonds, A. L. Vázquez De Parga, M. S. Fuhrer, D. K. Gaskill, *Adv. Mater. Interfaces* **2021**, *8*, 2101598.
- [33] A. Bansal, N. Nayir, K. Wang, P. Rondonanski, S. Subramanian, S. Kumari, J. A. Robinson, A. C. T. Van Duin, J. M. Redwing, *ACS Nano* **2023**, *17*, 230.
- [34] Y. Liu, X. Liu, C.-Z. Wang, Y. Han, J. W. Evans, A. Lii-Rosales, M. C. Tringides, P. A. Thiel, *J. Phys. Chem. C* **2021**, *125*, 6954.
- [35] J. R. Rumble, in *CRC Handbook of Chemistry and Physics*, 103rd ed., CRC Press/Taylor & Francis, Boca Raton, FL, **2021**, Ch. 2.
- [36] W. F. Gale, T. C. Totemeier, in *Smithells Metals Reference Book*, 8th ed., Elsevier Butterworth-Heinemann, Oxford, **2004**, Ch. 14.
- [37] J.-H. Kim, J. H. Hwang, J. Suh, S. Tongay, S. Kwon, C. C. Hwang, J. Wu, J. Young Park, *Appl. Phys. Lett.* **2013**, *103*, 171604.
- [38] R. D. Rodriguez, Z. Khan, B. Ma, A. Mukherjee, P. Meszmer, J. Kalbacova, E. Garratt, H. Shah, J. Heilmann, A. R. Hight Walker, B. Wunderle, E. Sheremet, M. Hietschold, D. R. T. Zahn, *Phys. Status Solidi (a)* **2019**, *216*, 1900055.
- [39] P.-C. Chen, W.-C. Miao, T. Ahmed, Y.-Y. Pan, C.-L. Lin, S.-C. Chen, H.-C. Kuo, B.-Y. Tsui, D.-H. Lien, *Nanoscale Res. Lett.* **2022**, *17*, 30.
- [40] H. Das, S. Sunkari, H. Naas, *ECS Trans.* **2017**, *80*, 239.
- [41] The Identification of Commercial Equipment or Vendor is not Intended to Imply Recommendation or Endorsement by NIST, nor is it Intended to Imply that the Materials or Equipment Identified are Necessarily the best Available for the Purpose.
- [42] R. M. Tromp, J. B. Hannon, A. W. Ellis, W. Wan, A. Berghaus, O. Schaff, *Ultramicroscopy* **2010**, *110*, 852.
- [43] R. M. Tromp, J. B. Hannon, W. Wan, A. Berghaus, O. Schaff, *Ultramicroscopy* **2013**, *127*, 25.
- [44] F. Niefind, H. G. Bell, T. Mai, A. R. Hight Walker, R. E. Elmquist, S. Pookpanratana, *J. Appl. Phys.* **2022**, *131*, 015303.
- [45] P. Rosenzweig, U. Starke, *Phys. Rev. B* **2020**, *101*, 201407.
- [46] P. Giannozzi, S. Baroni, N. Bonini, M. Calandra, R. Car, C. Cavazzoni, D. Ceresoli, G. L. Chiarotti, M. Cococcioni, I. Dabo, A. Dal Corso, S. de Gironcoli, S. Fabris, G. Fratesi, R. Gebauer, U. Gerstmann, C. Gougoussis, A. Kokalj, M. Lazzeri, L. Martin-Samos, N. Marzari, F. Mauri, R. Mazzarello, S. Paolini, A. Pasquarello, L. Paulatto, C. Sbraccia, S. Scandolo, G. Sclauzero, A. P. Seitsonen, et al., *J. Phys.: Condens. Matter* **2009**, *21*, 395502.
- [47] P. E. Blöchl, *Phys. Rev. B* **1994**, *50*, 17953.
- [48] G. Kresse, D. Joubert, *Phys. Rev. B* **1999**, *59*, 1758.
- [49] J. P. Perdew, K. Burke, M. Ernzerhof, *Phys. Rev. Lett.* **1996**, *77*, 3865.
- [50] J. P. Perdew, K. Burke, M. Ernzerhof, *Phys. Rev. Lett.* **1997**, *78*, 1396.
- [51] S. Rajabpour, Q. Mao, N. Nayir, J. A. Robinson, A. C. T. Van Duin, *J. Phys. Chem. C* **2021**, *125*, 10747.
- [52] W. Zhang, A. C. T. Van Duin, *Chem. Mater.* **2020**, *32*, 8306.
- [53] W. Zhu, H. Gong, Y. Han, M. Zhang, A. C. T. Van Duin, *J. Phys. Chem. C* **2020**, *124*, 12512.
- [54] AMS, *SCM, Theoretical Chemistry*, Vrije Universiteit: Amsterdam, The Netherlands, **2020**, 1.
- [55] W. Humphrey, A. Dalke, K. Schulten, *J. Mol. Graph.* **1996**, *14*, 33.
- [56] A. Stukowski, *Modell. Simul. Mater. Sci. Eng.* **2010**, *18*, 015012.
- [57] K. Momma, F. Izumi, *J. Appl. Crystallogr.* **2011**, *44*, 1272.
- [58] W. Li, L. Huang, M. C. Tringides, J. W. Evans, Y. Han, *J. Phys. Chem. Lett.* **2020**, *11*, 9725.
- [59] Y. Orimoto, K. Otsuka, K. Yagyū, H. Tochiara, T. Suzuki, Y. Aoki, *J. Phys. Chem. C* **2017**, *121*, 7294.
- [60] Y. Han, J. W. Evans, M. C. Tringides, *Phys. Rev. Mater.* **2021**, *5*, 074004.